Functional and Mechanical Characteristics of Ultrafine-Grained Fe-Mn-Si Alloys for Biomedical Applications

O. V. Rybalchenko¹*, N. S. Martynenko¹, G. V. Rybalchenko², E. A. Lukyanova¹, V. S. Komarov^{1,3}, M. A. Kaplan¹, A. N. Belyakov⁴, P. D. Dolzhenko⁴, I. V. Shchetinin³, A. G. Raab⁵, S. V. Dobatkin¹, and S. D. Prokoshkin³

¹ Baikov Institute of Metallurgy and Materials Science, Russian Academy of Sciences, Moscow, 119334 Russia

² Lebedev Physical Institute, Russian Academy of Sciences, Moscow, 119991 Russia

³ National University of Science and Technology "MISIS", Moscow, 119049 Russia

⁴ Belgorod National State University, Belgorod, 308015 Russia

⁵ Institute of Molecule and Crystal Physics, Ufa Federal Research Center, Russian Academy of Sciences, Ufa, 450075 Russia

* e-mail: rybalch@mail.ru

Received February 1, 2024; revised April 11, 2024; accepted April 12, 2024

Abstract—This work examines the possibility of regulating the corrosion rate of Fe-Mn-Si alloys by modifying their structure via equal channel angular pressing. It is found that the formed ultrafine-grained austenitic structure of Fe-Mn-Si alloys leads to a significant increase in strength characteristics at satisfactory ductility. The presence of special twin boundaries in the structure of Fe-Mn-Si alloys improves their corrosion resistance, while a predominantly grain-subgrain structure in the absence of twin boundaries increases the corrosion rate up to 0.4 mm/year. The shape memory effect in the studied alloys manifests itself at temperatures unacceptable for medical use. Structure refinement by equal channel angular pressing in modes that ensure a completely austenitic state leads to a decrease in shape memory properties.

Keywords: Fe-Mn-Si alloys, equal channel angular pressing, shape memory effect, microstructure, microhardness, mechanical properties, corrosion rate

DOI: 10.1134/S1029959924060080

1. INTRODUCTION

In recent years, considerable study has been given to biodegradable alloys, including iron-based ones [1, 2]. The idea of using such alloys as temporary (biodegradable) medical implants, when the dissolving material is replaced by newly formed tissue, is attractive in terms of increasing the treatment efficiency and reducing the patient discomfort. Such implants may be in demand, for example, in orthopedics for osteosynthesis or in cardiovascular surgery [2–9]. Iron-based alloys have a strength comparable to stainless steels but a low biodegradation rate, so their development focuses on increasing this parameter. An effective method of controlling the degradation rate is alloying [10, 11]. In this case, the strategy was to add more electronegative metals to increase the susceptibility of the matrix to corrosion, as well as more noble metals to form intermetallic phases. Such phases act as cathodes with respect to the matrix, causing microgalvanic corrosion [12]. This strategy was confirmed in [7–9] for the Fe-Mn system, where the addition of Mn allowed to lower the standard electrode potential of the alloy and increase its degradation rate, as well as in [13, 14] using the additional Pd alloying element.

The use of Fe-Mn-Si alloys for medical applications was first proposed in [15]. In a certain compositional range, close to ~30% Mn and ~5% Si (hereinafter wt%), these alloys have a pronounced shape memory effect [16, 17]. In Fe-Mn-Si alloys, this effect is caused by the $\gamma(\text{fcc}) \rightarrow \epsilon(\text{hcp})$ martensitic transformation with the reverse transformation upon heating, as opposed to thermoelastic martensitic transformation in most shape memory alloys, including iron-

based ones[16–19]. In this case, the shape recovers at very high temperatures, which does not allow these alloys to be used in medicine. A shift of the start temperature of direct martensitic transformation M_s in these alloys to the temperature range of the human body could soften the crystal lattice in this temperature range and consequently decrease the elastic modulus. This effect is even more important for manufacturing implantable devices for osteosynthesis than the shape memory effect because a decrease in Young's modulus increases the biomechanical compatibility of the implant and human bone. Silicon is also an important microelement for osteogenesis [20, 21].

In [15, 22], the Fe–30% Mn–6% Si alloy was compared with pure iron and the Fe–30% Mn alloy [15]. The authors used the potentiodynamic polarization method to show that the strong and ductile silicon-containing alloy had the lowest corrosion potential and the highest corrosion current density. This means that the alloy is characterized by a lower corrosion resistance, which can be explained by the worse corrosion resistance of austenite and ε martensite compared to ferrite [22]. In addition, this alloy was found to have a satisfactory in vitro biocompatibility [15].

Works [23, 24] studied the in vivo biocompatibility of Fe-Mn-Si alloys of different compositions. The in vivo experiments on Wistar rats [23] revealed a very good biocompatibility of the subdermal implant with the normal metabolism of the resulting products and showed that bone implants made of Fe-Mn-Si alloy ensured normal healing of bone fractures. In vivo tests on a rabbit tibia model for 28 days showed a higher osteoinductive and osteoconductive capacity of the implant made of Fe-10Mn-6Si-1Ca alloy compared to the reference Fe-10Mn-6Si alloy [23]. At the same time, the alloys were found to be low biodegradable [23, 24].

In further works [25–28], attempts were made to improve the composition and processing modes of Fe-Mn-Si alloys to achieve the required corrosion rate for bioresorbable implants. It was confirmed that the corrosion rate of Fe-based alloys increased with increasing Mn content. Thus, the corrosion rate of Fe-Mn-5Si alloys increases to 0.48, 0.59, and 0.80 mm/year with increasing Mn content to 23, 26, and 30%, respectively [25]. In [25], it was shown that effective homogenizing heat treatment of the Fe–30% Mn–5% Si alloy decreased the martensite start temperature $M_{\rm s}$ to 60°C and reduced Young's modulus by half compared to that of pure iron (to

100 GPa). However, despite a significant number of studies [25-28], no solution has been found to the problem of increasing the corrosion rate at the start temperature of reversible $\gamma \leftrightarrow \epsilon$ martensitic transformation M_s close to the temperature of the human body. In [29], from dynamic indentation tests measuring the indentation depth as a function of the indentation load, it was found that equal channel angular pressing (ECAP) of Fe-29% Mn-5% Si alloy at 400°C reduced Young's modulus by more than 2.6 times: from 173.3 ± 9 GPa in the annealed state to 65.9 ± 2 GPa. The reason for this can be a nanostructured state formed in the ECAP-treated alloy. However, the effect of ECAP on the shape memory effect and the temperature of direct and reverse martensitic transformations was given no consideration in this work. The obtained results indicated the highest biomechanical compatibility of the alloy thus treated as compared to most other medical alloys (except for Mg-based alloys whose Young's modulus (~45 GPa) is the closest to that of cortical bone (10–20 GPa)).

The current state of research shows great scientific interest in studying biodegradation processes of Fe-Mn-Si alloys to increase their corrosion rate and biomechanical compatibility. In this connection, the objects of investigation are Fe-29Mn-3.7Si and Fe-29Mn-5Si alloys, whose compositions are close to the optimum composition of shape memory alloys. The corrosion rate is controlled by modifying the alloy structure by equal channel angular pressing. The aim of this work is to determine the influence of the ultrafine-grained structure of the Fe-29Mn-5Si and Fe-29Mn-3.7Si alloys produced by ECAP on the mechanical properties, corrosion rate, as well as the shape memory effect previously unstudied in such alloys.

2. MATERIALS AND METHODS

The materials to be studied were Fe-29Mn-3.7Si and Fe-29Mn-5Si alloys melted and remelted up to 10 times in a Leybold Gereus L200DI vacuum arc furnace from commercially pure iron, electrolytic manganese (99.8% Mn), and single-crystal silicon (99.99% Si). The chemical composition of the alloys is presented in Table 1. The derived castings were forged at 1100°C to obtain rods ~16 mm in diameter.

Then, the alloy rods were homogenized at 1100°C for 12 h in vacuum quartz tubes with subsequent water cooling. The annealed rods were used to cut billets 6 cm in length and 10 mm in diameter. Equal channel angular pressing was carried out along the

Table 1. Chemical composition of the studied alloys

Allow designation	Chemical composition, wt %			
Alloy designation	Mn	Si	Fe	
Fe-Mn-5Si	28.9	5.12	Base	
Fe-Mn-3.7Si	29	3.7	Base	

Bc route at the temperatures 300 and 400°C in the matrix with channels intersecting at an angle of 120°. This allowed the Fe-Mn-3.7Si alloy to be deformed in 4 passes of ECAP. The Fe-Mn-5Si alloy was deformed in the isothermal mode by 4 passes of ECAP at 400°C and in the stepwise ECAP mode consisting of 4 passes at 300°C and 1 pass at 450°C. The equivalent total strain of the specimens calculated for the given geometry of the tool was 3.6 after 4 passes of ECAP and 4.5 after 5 passes of ECAP.

The initial structure of annealed alloys was studied under an ADF I350 optical microscope and a JEOL JSM-7001F scanning electron microscope. The average grain size was calculated using the NEXSYS Image Expert Prof 3 program. The grain size was measured by the random linear intercept method in at least 15 fields of view. X-ray diffraction analysis of alloys was made with a Rigaku Ultima IV diffractometer using CoK_{α} radiation (the wavelength λ = 0.17902 nm). X-ray diffraction patterns were analyzed using the Rietveld method implemented in Rigaku PDXL2 software and the PDF-2 database (ICDD). Instrumental broadening was taken into account by imaging the LaB6 standard. Substructural parameters were calculated and microstrains were converted into the dislocation density by the method implemented in PDXL2 software [30]. The alloy structure after deformation was studied by transmission electron microscopy using a JEOL JEM 2100 electron microscope. Phase transformations during heating/cooling were determined using a Mettler-Toledo DSC 3+ differential scanning calorimeter with a cooling/heating cycle in the temperature range from -100 to 200°C at the heating/cooling rate 10 °C/min in an argon atmosphere.

Uniaxial tensile tests were performed at room temperature on an Instron 3380 machine with the load $100 \, \text{kN}$ and the crosshead speed $1 \, \text{mm/min}$. Tensile specimens with the gauge length $5.75 \, \text{mm}$ and cross section $2 \times 1 \, \text{mm}^2$ were spark cut from billets in the initial state and after equal channel angular pressing. The specimens were mechanically ground using sandpaper of different grit sizes and polished with diamond paste. Microhardness was measured using a

Wolpert Wilson 402 MVD microhardness tester by the Vickers method under the load 0.1 kgf for 15 s. At least ten measurements were made for each group of specimens.

Reversible strain and the degree of shape recovery were determined by the thermomechanical method consisting in the deformation to a given strain by the bending scheme. Specimens were heated above the shape recovery temperature, and residual strain was measured. Reversible strain was defined as the difference between induced and residual strain. The degree of shape recovery was defined as the ratio of reversible to induced strain. In addition, reactive stresses arising during heating were determined by deforming the specimen by 3% according to the uniaxial tension scheme with subsequent heating to the shape recovery temperature (about 300°C) and recording changes in stresses. Then the specimen was cooled, and true reactive stresses were calculated.

The corrosion rate was studied by the potentiodynamic polarization method using a BioLogic SAS SP-300 potentiostat. Use was made of a flat cell with three electrodes, one of which was the studied specimen. The specimen was ground and mirror polished. A silver chloride (Ag/AgCl) electrode was used as the reference electrode, and a platinum grid was used as the auxiliary electrode. Corrosion studies were carried out in a physiological solution of 0.9% NaCl with a pH of 7.4. Corrosion was studied at room temperature with the scan rate 1 mV/s. The open circuit potential measurement time was 20 min. Corrosion potential, corrosion current density, and corrosion rate C_R were calculated using BioLogic EC-Lab software in accordance with ASTM G59-23 using the following equation:

$$C_{\rm R} = \frac{3.27 \times 10^{-3} i_{\rm cor} EW}{\rho S},$$

where C_R is the corrosion rate, mm/year, i_{cor} is the corrosion current density calculated from the polarization curve, $\mu A \text{ cm}^{-2}$, EW is the equivalent weight, g/eq, ρ is the alloy density, g/cm³.

Immersion tests were run in Dulbecco's Modified Eagle Medium (DMEM) in accordance with ASTM G31-21. Mirror polished test specimens had the shape of quarter disks 10 mm in diameter and up to 1 mm in thickness. Each test was performed on three alloy specimens in the annealed state and after different ECAP modes. The specimens were immersed in 70% ethanol for 2 h, dried, and immersed in 1 ml of the culture medium at 37°C. After 1 and 14 days, the specimens were taken out of the solution and, after

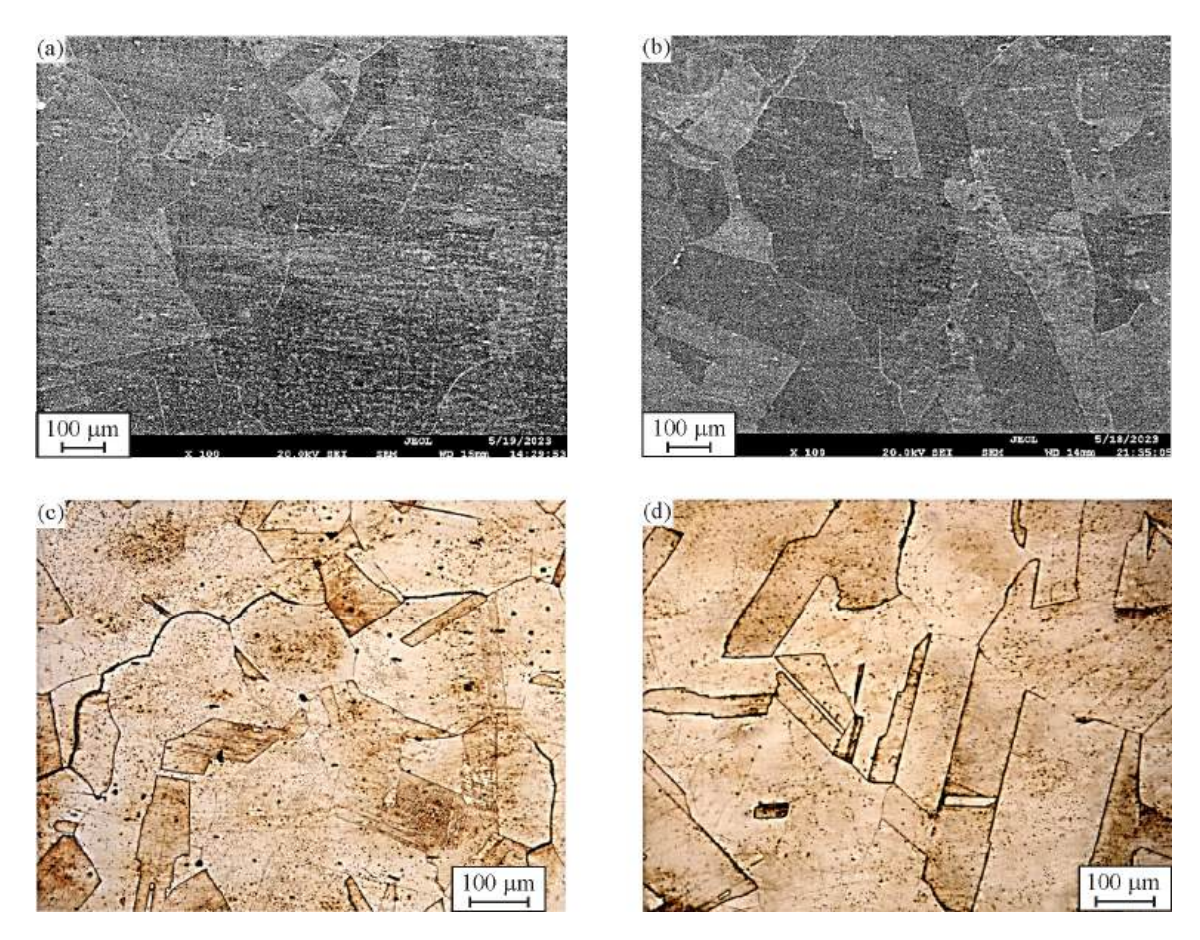


Fig. 1. Microstructure of Fe-Mn-3.7Si (a, c) and Fe-Mn-5Si (b, d) alloys after homogenizing annealing. Scanning electron microscopy (a, b) and optical microscopy (c, d) (color online).

removing the corrosion products, washed with distilled water and dried at room temperature. Before and after the immersion tests, the specimens were weighed on a Sartorius M2P Pro 11 microbalance. The degradation rate was determined using the formula

$$C\Delta m = \frac{8.76 \times 10^4 (m_0 - m_{\tau})}{S\rho\tau} \text{ mm/year,}$$

where m_0 and m_{τ} are the initial and final masses of the specimens, respectively, S is the corroded surface area, cm², τ is the test duration, h, and ρ is the alloy density, g/cm³.

3. RESULTS AND DISCUSSION

3.1. Microstructure of Fe-Mn-Si Alloys in the Annealed State and after Equal Channel Angular Pressing

The initial structure of the studied alloys is shown in Fig. 1. The Fe-Mn-3.7Si alloy after forging and annealing has a coarse-grained microstructure with grains $201\pm21\,\mu m$ in size and annealing twins $24\pm$

 $8~\mu m$ in thickness (Figs. 1a, 1c). In the Fe-Mn-5Si alloy, the structure consists of grains $160\pm12~\mu m$ in size and annealing twins $37\pm5~\mu m$ in thickness (Figs. 1b, 1d).

The Fe-Mn-3.7Si alloy after 4 passes of ECAP at 300°C (Figs. 2a–2c) and 400°C (Figs. 2d–2e) had an ultrafine-grained austenitic microstructure. During ECAP at 300°C , such a structure forms in 152 ± 25 nm thick shear bands when they are crossed by dislocation walls (Figs. 2a, 2b) and thin twins with the average thickness 16 ± 3 nm (Fig. 2c). According to transmission electron microscopy, the dislocation density inside grains and subgrains exceeds $2\times10^{15}\,\text{cm}^{-2}$. With an increase in the deformation temperature to 400°C , the twin density increases. The structure becomes predominantly twinned with the average twin thickness of 22 ± 5 nm in a highly defective austenitic structure.

In the Fe-Mn-5Si alloy specimens after stepwise ECAP, a nanostructure with the average size of structural elements of 97.7 ± 5 nm and small areas of thin

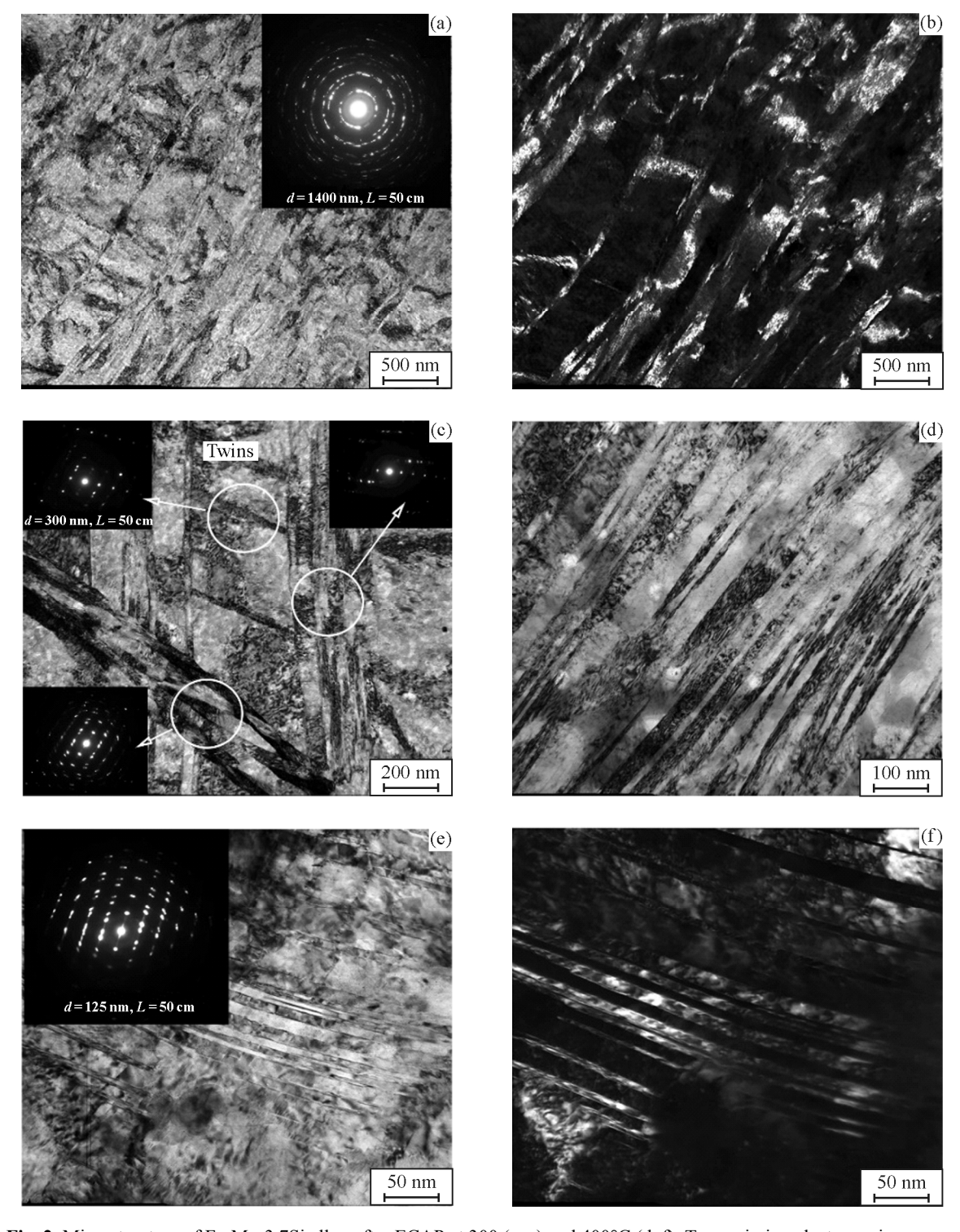


Fig. 2. Microstructure of Fe-Mn-3.7Si alloy after ECAP at 300 (a-c) and 400°C (d-f). Transmission electron microscopy.

twins (\sim 8.0±0.5 nm) was formed starting from the initial deformation temperature 300°C with further increasing up to 450°C (Figs. 3a–3c). In the specimens after ECAP at 400°C, the structure of the Fe-Mn-5Si alloy forms in the same way as in the low-Si alloy due

to twinning in austenite ($\sim 11\pm 1\,\text{nm}$) (Figs. 3d–3e) with rare areas of high-density dislocations, inside which nanograins are formed (Fig. 3e). According to transmission electron microscopy, the dislocation density within such zones exceeds $4\times 10^{15}\,\text{cm}^{-2}$.

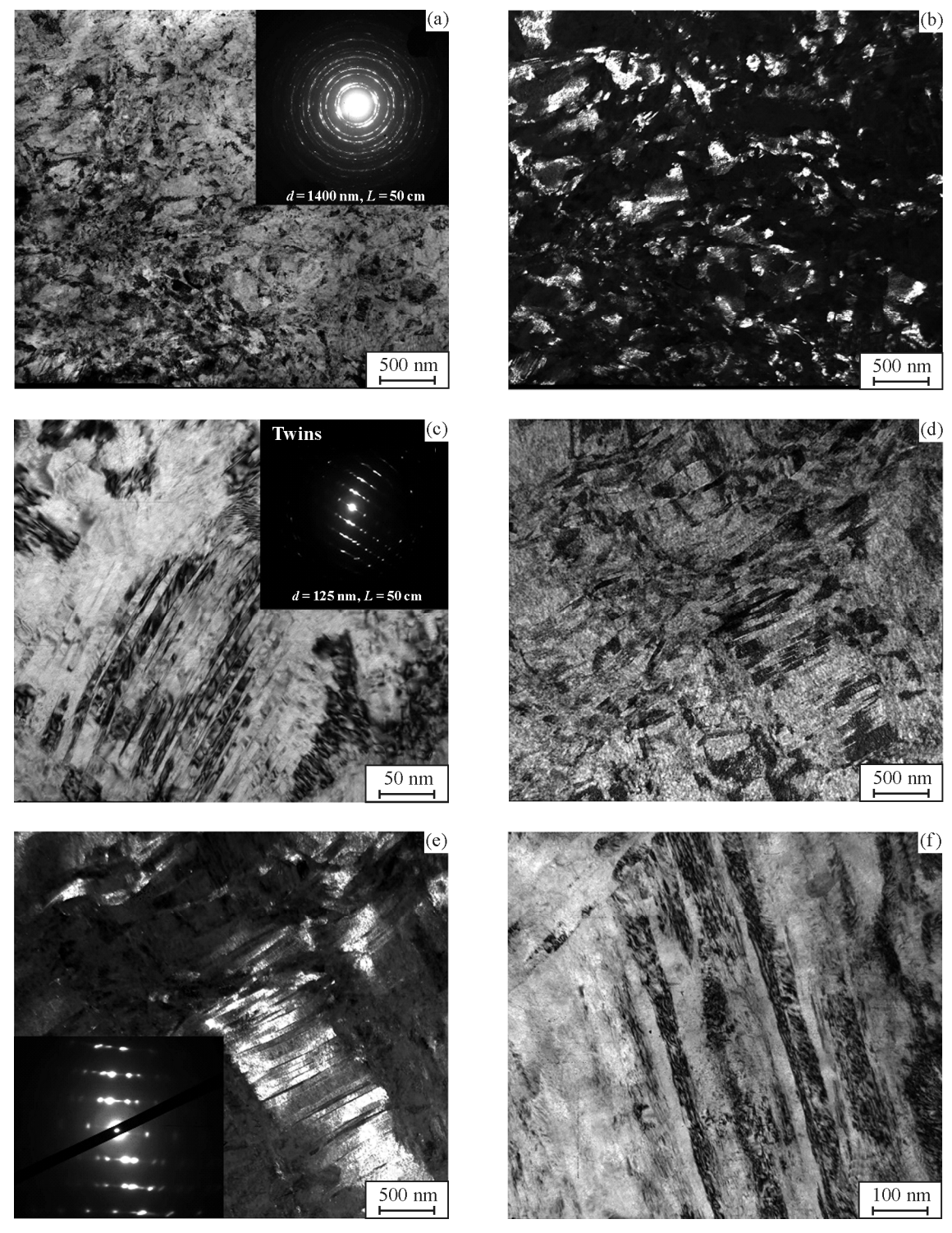
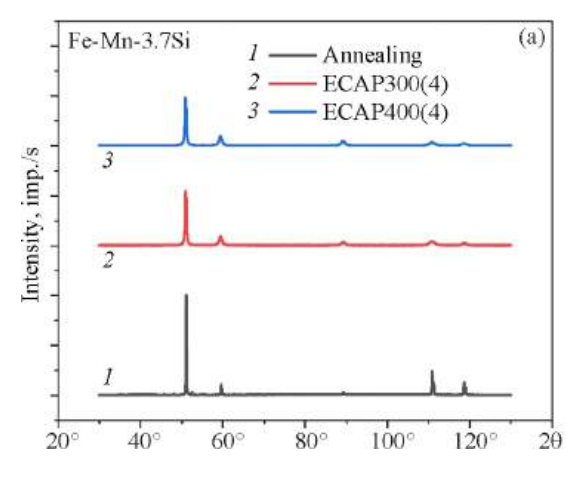


Fig. 3. Microstructure of Fe-Mn-5Si alloy after 4 passes of ECAP at 300°C + 1 pass of ECAP at 450°C (a–c) and 4 passes of ECAP at 400°C (d–f). Transmission electron microscopy.

3.2. X-Ray Diffraction Analysis of Fe-Mn-Si Alloys after Annealing and Equal Channel Angular Pressing

X-ray phase analysis revealed a fully austenitic structure of the alloys both before and after deforma-

tion (Fig. 4, Table 2). Analysis of line broadening showed only the microstrain component (Table 2). The dislocation density calculated from the microstrains obtained by the complete fitting of the diffraction profile by the Rietveld method showed that



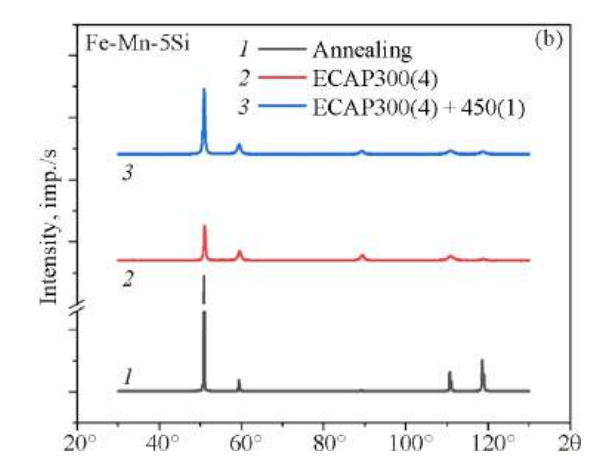


Fig. 4. X-ray phase analysis of Fe-Mn-3.7Si (a) and Fe-Mn-5Si (b) alloys after annealing and ECAP (color online).

ECAP was accompanied by a significant (more than 100 times) increase in the dislocation density.

3.3. Mechanical Properties and Microhardness of Fe-Mn-Si Alloys after Annealing and Equal Channel Angular Pressing

As for tensile properties (Fig. 5), an insignificant difference in the silicon content (3.7 and 5% Si) predetermined the same strength characteristics ($\sigma_B \sim 700\,\text{MPa}$) of the annealed alloys but different ductility: $\delta = 55.5 \pm 6\%$ for the alloy with 3.7% Si and $\delta = 32 \pm 0.5\%$ for the alloy with 5% Si in the initial state. The same occurs after deformation by ECAP at 400°C. The tensile strength of both silicon-containing alloys remains at the same level, increasing two-fold above that in the initial annealed state ($\sigma_B \sim 1400\,\text{MPa}$). In this case, the relative elongation decreases to 14% for the alloy with 3.7% Si and to 10.8% for the alloy with 5% Si. The difference in the silicon content by 1.4% has no effect on the strength

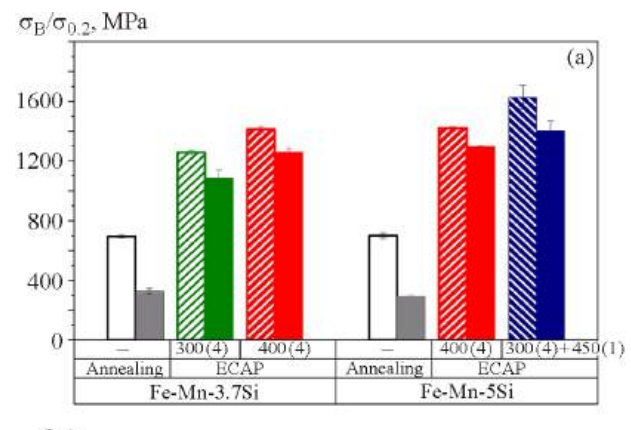
characteristics of the studied alloys but decreases their ductility with increasing silicon content. The best mechanical properties were obtained for the Fe-Mn-5Si alloy after stepwise ECAP starting with the temperature 300°C (4 passes) and increasing to 450°C. The tensile strength of the alloy increased to 1626 ± 79 MPa, and the yield strength improved to 1403 ± 66 MPa at the satisfactory ductility $\delta=8.5$ %.

Vickers hardness tests showed that ECAP increased the microhardness by more than 1.5 times for the Fe-Mn-3.7Si alloy and more than 2 times for the Fe-Mn-5Si alloy compared to the annealed state (Fig. 6), which, along with the mechanical properties, indicates significant structural changes.

Such high tensile strength at relatively low (8.5–14%) relative elongation seems unacceptable for medical applications. However, in special clinical applications, the strength of the material must correspond to the cross-sectional area of the used device, such as a pin for osteosynthesis. For example, according to the general specification for metal skeletal pins (ISO)

Table 2 Phase c	omnosition and	microstrain	of Fe-Mn-	Si allovs afte	er annealing and ECAP
Table 2. Thase c	ombosinon and	microsuam	OI I C-IVIII-	oi anovs and	i annicannig and ECAi

Alloy	Treatment	Phase	Space group	Period, nm	Volume fraction, vol %	Microstrain ε, %	Dislocation density, cm ⁻²
7Si	Annealing	γ	225: Fm3m	0.3605(2)	100(5)	0.02(1)	1 × 10 ⁹
Fe-Mn-3.7Si	4 passes of ECAP at 300°C	γ	225: Fm3m	0.3606(3)	100(5)	0.30(1)	3.5×10^{11}
Fe-J	4 passes of ECAP at 400°C	γ	225: Fm3m	0.3603(3)	100(6)	0.34(1)	4.6×10^{11}
Si	Annealing	γ	225: Fm3m	0.3604(10)	100	0.04(2)	1 × 10 ⁹
Fe-Mn-5Si	4 passes of ECAP at 400°C	γ	225: Fm3m	0.3604(4)	100	0.47(1)	8.7×10^{11}
	4 passes of ECAP at 300°C + 1 pass of ECAP at 450°C	γ	225: Fm3m	0.3599(3)	100(2)	0.41(1)	6.7 × 10 ¹¹



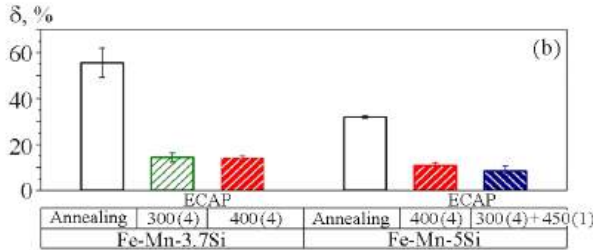


Fig. 5. Mechanical properties of Fe-Mn-3.7Si and Fe-Mn-5Si alloys in the initial state and after different ECAP modes. Strength characteristics (a) and relative elongation (b) (color online).

5838-1) made of wrought stainless steel, which are intended to replace biodegradable Fe-Mn-based alloys, the tensile strength can reach more than 1400 MPa depending on the part diameter at the minimum elongation 3%. In addition, the high specific strength of iron-based alloys allows miniaturizing the implanted product, thus reducing the negative impact on the human body, and regulating the biodegradation rate of this part.

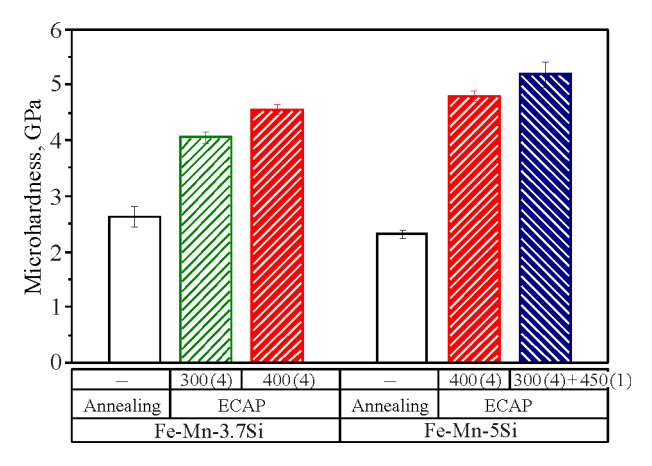


Fig. 6. Microhardness of Fe-Mn-3.7Si and Fe-Mn-5Si alloys in the initial state and after different ECAP modes (color online).

3.4. Differential Scanning Calorimetry of Fe-Mn-Si Alloys after Annealing and Equal Channel Angular Pressing

Since the shape memory effect in Fe-Mn-Si alloys is realized due to heat-induced reverse transformation of ε martensite formed during the stress-induced direct $\gamma(\text{fcc}) \rightarrow \varepsilon(\text{hcp})$ martensitic transformation, it was necessary to determine the critical start and finish temperatures of direct martensitic transformation ($M_{\rm s}$ and $M_{\rm f}$) upon cooling and reverse martensitic transformation ($A_{\rm s}$ and $A_{\rm f}$) upon heating. Figure 7 shows calorimetric curves of the alloys after annealing and after ECAP in the studied modes.

For the Fe-Mn-3.7Si alloy in the initial annealed state, a small peak (48.8°C) was observed on the DSC curve upon cooling, which was related to the martensitic transformation in the temperature range $M_s = 64.7$ °C and $M_f = -4.5$ °C. To interpret the heat flux, the released heat was calculated, which was 1.1 J/g, indicating a weak intensity of the transformation. The DSC curves have peaks at similar temperatures with heat absorption of the same order (-0.96 and 1.28 J/g) upon heating and upon reheating, but no endothermic peaks corresponding to reverse martensitic transformation were found up to the temperature 300°C. For the Fe-Mn-3.7Si alloy after 4 passes of ECAP at 400°C, a peak was observed on the DSC curve upon cooling at 34.5°C, which was related to martensitic transformation in the temperature range $M_s = 85.2$ °C and $M_f = -9$ °C, corresponding to the released heat 4.8 J/g. After ECAP at 300°C, no pronounced peaks were found on the DSC curve of the Fe-Mn-3.7Si alloy either upon heating or upon cooling.

For the Fe-Mn-5Si alloy in the annealed state, peaks were present on the DSC curve both upon cooling and upon heating. The peak of martensitic transformation was observed at 13°C in the temperature range $M_s = 28^{\circ}\text{C}$ and $M_f = -14^{\circ}\text{C}$. Reverse martensitic transformation was in the range of high temperatures $A_s = 117$ °C and $A_f = 180$ °C, and its peak at 148.8°C corresponded to the absorbed heat −1.3 J/g. During cooling after the first heating, small characteristic endothermic peaks were observed at the start and finish temperatures of reverse martensitic transformation. This temperature range of reverse martensitic transformation was marked by dashed vertical lines and was left for comparison on the graphs corresponding to heating and cooling of the Fe-Mn-5Si alloy after ECAP in the isothermal mode at 400°C and in the stepwise mode at 300°C with temperature

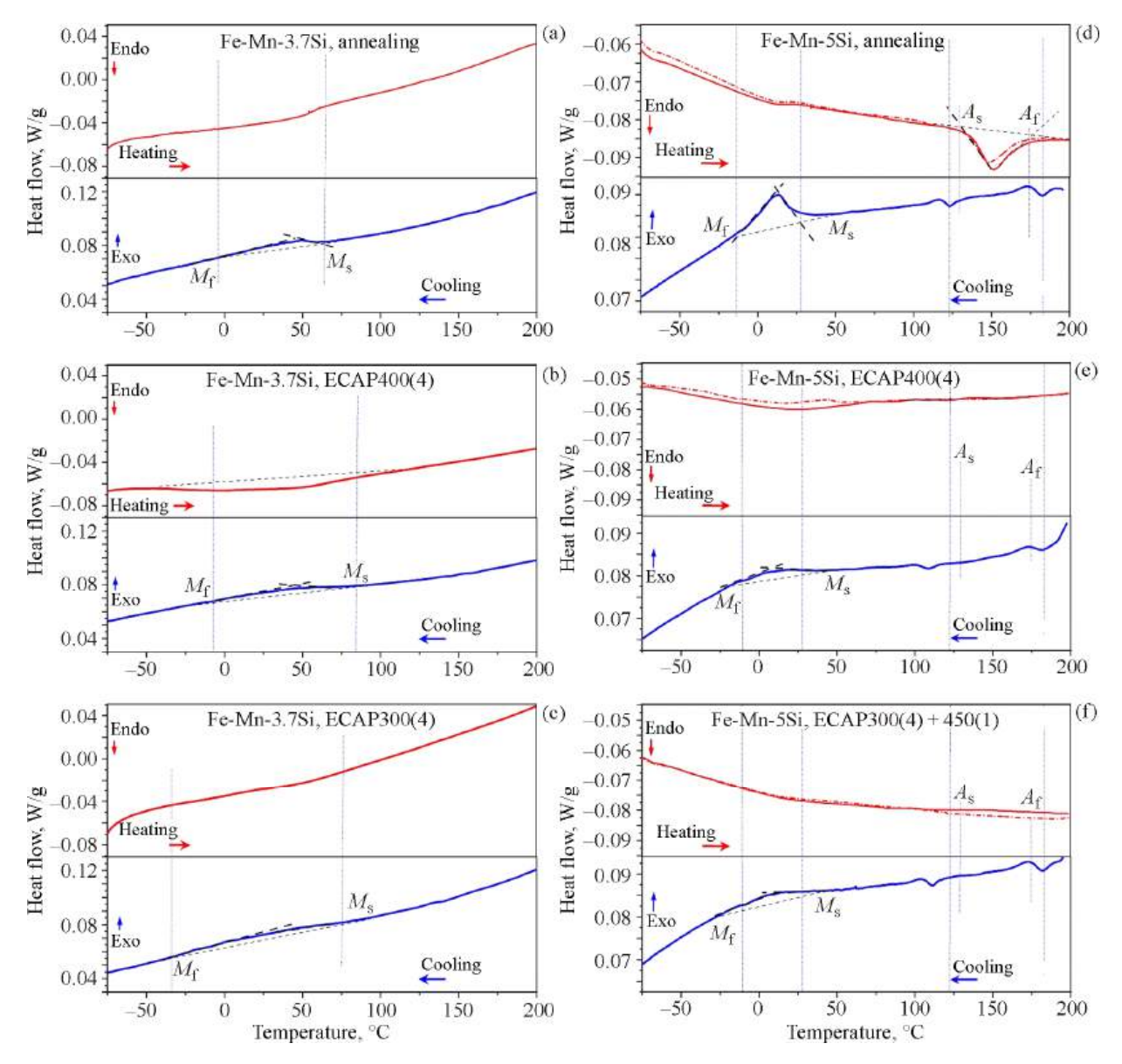


Fig. 7. Heat flow as a function of temperature for Fe-Mn-3.7Si (a–c) and Fe-Mn-5Si (d–e) alloys in the initial annealed state and after different ECAP modes. Differential scanning calorimetry (color online).

increase to 450°C. Assuming that these peaks mark the reverse martensitic transformation range, which is undetected on the DSC curve during heating, the finish temperature of reverse martensitic transformation $A_{\rm f}$ for the Fe-Mn-5Si alloy after ECAP in two modes does not change and remains equal to $A_{\rm f}$ = 180°C, while the start temperature $A_{\rm s}$ shifts toward lower values. However, these temperatures are still insufficiently low for the shape memory effect to be used in medical devices. The start temperature $M_{\rm s}$ of the Fe-Mn-5Si alloy after ECAP in two modes does not change and remains equal to 28°C.

3.5. Shape Memory Effect of Fe-Mn-Si Alloys after Annealing and Equal Channel Angular Pressing

Though the shape memory effect (direct and reverse martensitic transformation) in the studied alloys is realized at temperatures unacceptable for medical use, the study of shape memory properties remains an important task and is required for material certification.

The studied alloys were initially in the same phase state (austenite). Various treatments affected only their structural state (size of structural elements and

		Fe-Mn-3.7Si		Fe-Mn-5Si			
Shape memory characteristics	Annealing	4 passes of ECAP at 400°C	4 passes of ECAP at 300°C	Annealing	4 passes of ECAP at 400°C	4 passes of ECAP at 300°C + 1 pass of ECAP at 450°C	
Induced strain, %	3.7	3.3	2.8	3.7	3.1	2.8	
Reversible strain, %	1.2	0.1	0.2	0.8	0.6	0.5	
Shape recovery, %	32.4	3.0	7.1	21.6	19.4	17.9	
Induced strain, %	6.3	5.7	5.4	6.0	5.4	4.6	
Reversible strain, %	1.8	1.0	0.6	2.6	1.4	0.7	
Shape recovery, %	28.6	17.5	11.1	43.3	25.9	15.2	
Reactive stress at the strain 3%, MPa	60	48	17	51	15	32	

Table 3. Characteristics of the shape memory effect after annealing and ECAP in different modes

state of boundaries). Nevertheless, it is necessary to take into account the formation of ϵ martensite during deformation, which largely determines the shape memory effect in the material. The experimental values of induced strain were about 3% (2.8–3.7%) and about 6% (4.6–6.3%). The process was studied by heating the specimens above the shape recovery temperature and recording residual strain. Reversible strain was determined as the difference between induced and residual strain. The degree of shape recovery was equal to the ratio of reversible to induced

strain. In addition, reactive stresses arising during heating were determined by deforming the specimen by 3% according to the uniaxial tension scheme, heating to the shape recovery temperature (about 300°C), and recording changes in stresses. Then the specimen was cooled, and true reactive stresses were calculated (Table 3).

The characteristics of shape recovery and reactive stresses of alloys with different silicon contents after different treatments are shown in Fig. 8. It is found that annealed alloys with a coarse-grained structure

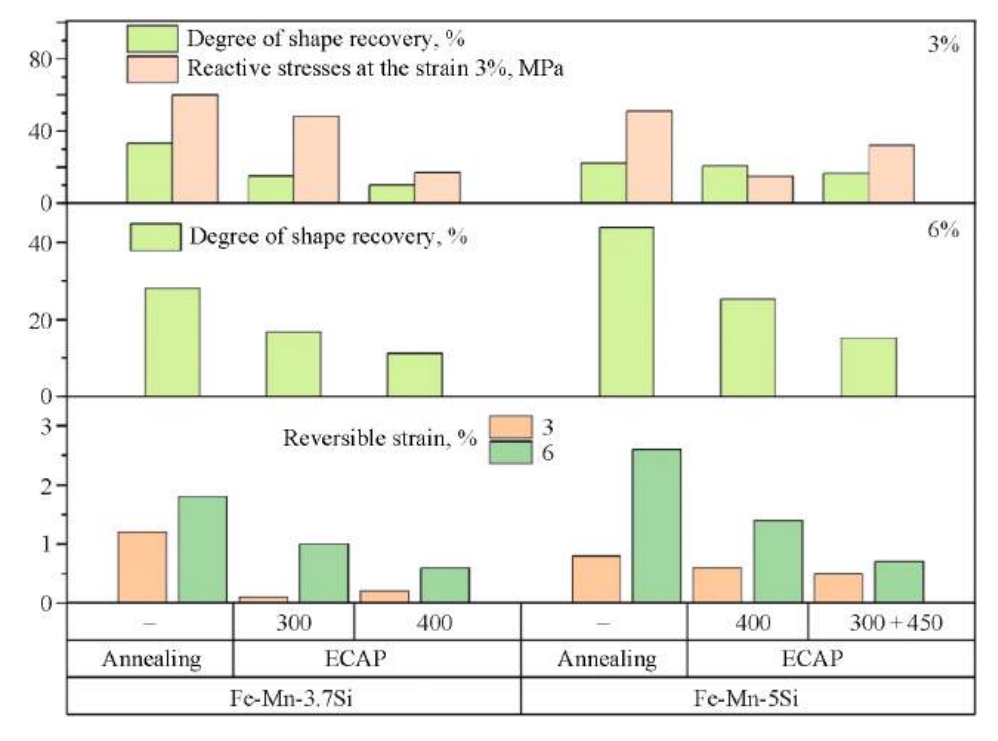


Fig. 8. Shape memory effect for Fe-Mn-3.7Si and Fe-Mn-5Si alloys in the initial state and after different ECAP modes (color online).

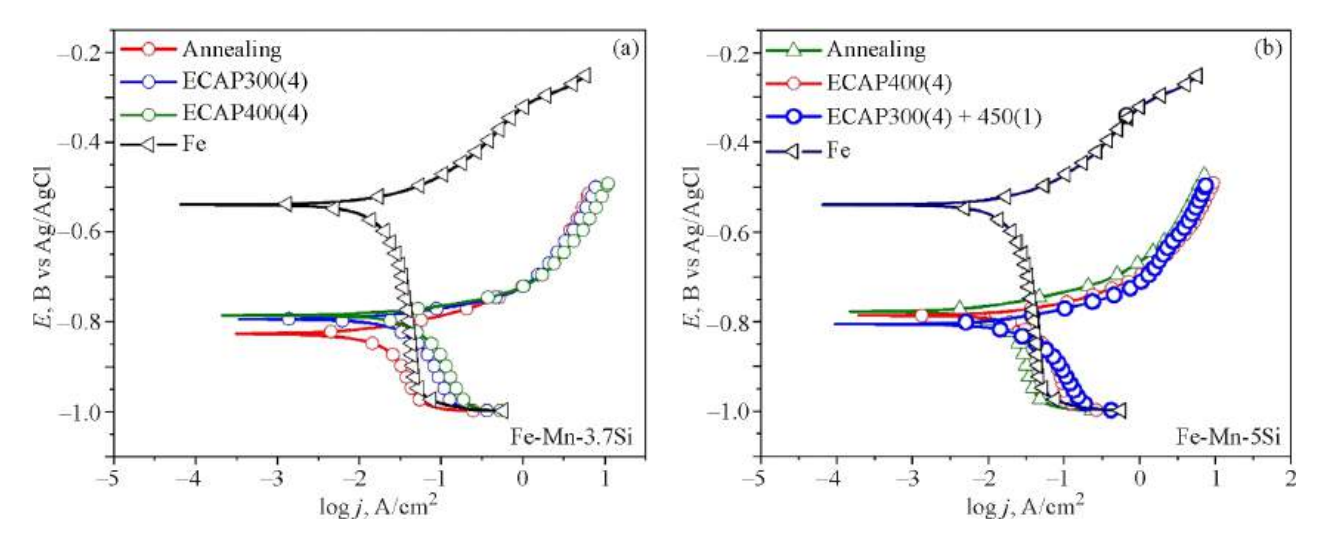


Fig. 9. Results of electrochemical corrosion: potentiodynamic polarization of Fe-Mn-3.7Si (a) and Fe-Mn-5Si (b) alloys in the initial state and after ECAP (Ag/AgCl reference electrode) (color online).

have the best shape recovery characteristics. The degree of shape recovery at the induced strain 3% are 22 and 33%, and the reactive stresses are 51 and 60 MPa for alloys containing 5 and 3.7% Si, respectively. An increase in induced strain from 3 to 6% leads to an increase in the degree of shape recovery in all cases. In the annealed specimens, the degree of shape recovery is 28 and 43% for alloys with 3.7 and 5% Si, respectively. An increase in the degree of shape recovery with increasing induced strain may be associated with the formation of a larger amount of ϵ martensite directly during deformation.

Equal channel angular pressing in the studied modes promotes significant refinement of the austenitic structure, which complicates the ε -martensite formation both during cooling and during reversible deformation and, as a consequence, significantly reduces

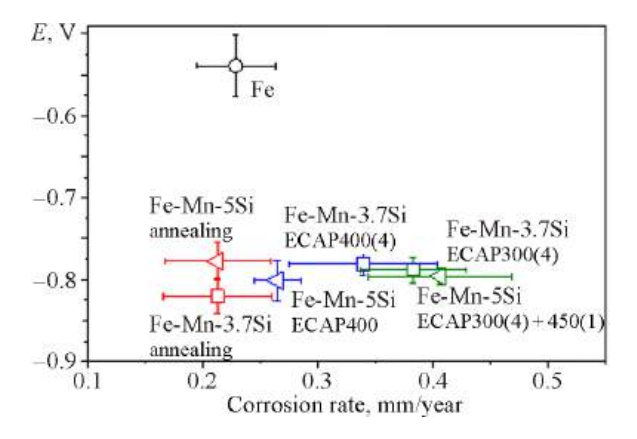


Fig. 10. Comparison of the results of potentiodynamic polarization in the alloys after annealing and ECAP (color online).

both the degree of shape recovery (to 3%) and reactive stresses (to 15 MPa). Nevertheless, at higher induced strains (6%), both the degree of shape recovery and reversible strain are higher in the alloy with 5% silicon. Thus, it was shown that structure refinement by ECAP in modes providing a fully austenitic state leads to a decrease in the shape memory properties.

3.6. Study of Electrochemical Corrosion of Fe-Mn-Si Alloys by the Potentiodynamic Polarization Method

Analysis of the potentiodynamic polarization curves revealed that alloying of iron with manganese

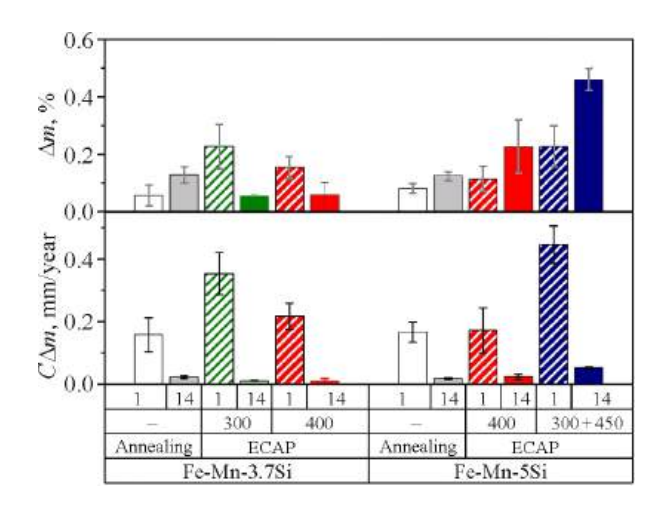


Fig. 11. Results of the immersion test based on determining the mass loss due to corrosion of Fe-Mn-3.7Si and Fe-Mn-5Si alloys in the initial state and after different ECAP modes. Δm is the mass loss, %; $C\Delta m$ is the corrosion rate, mm/year (color online).

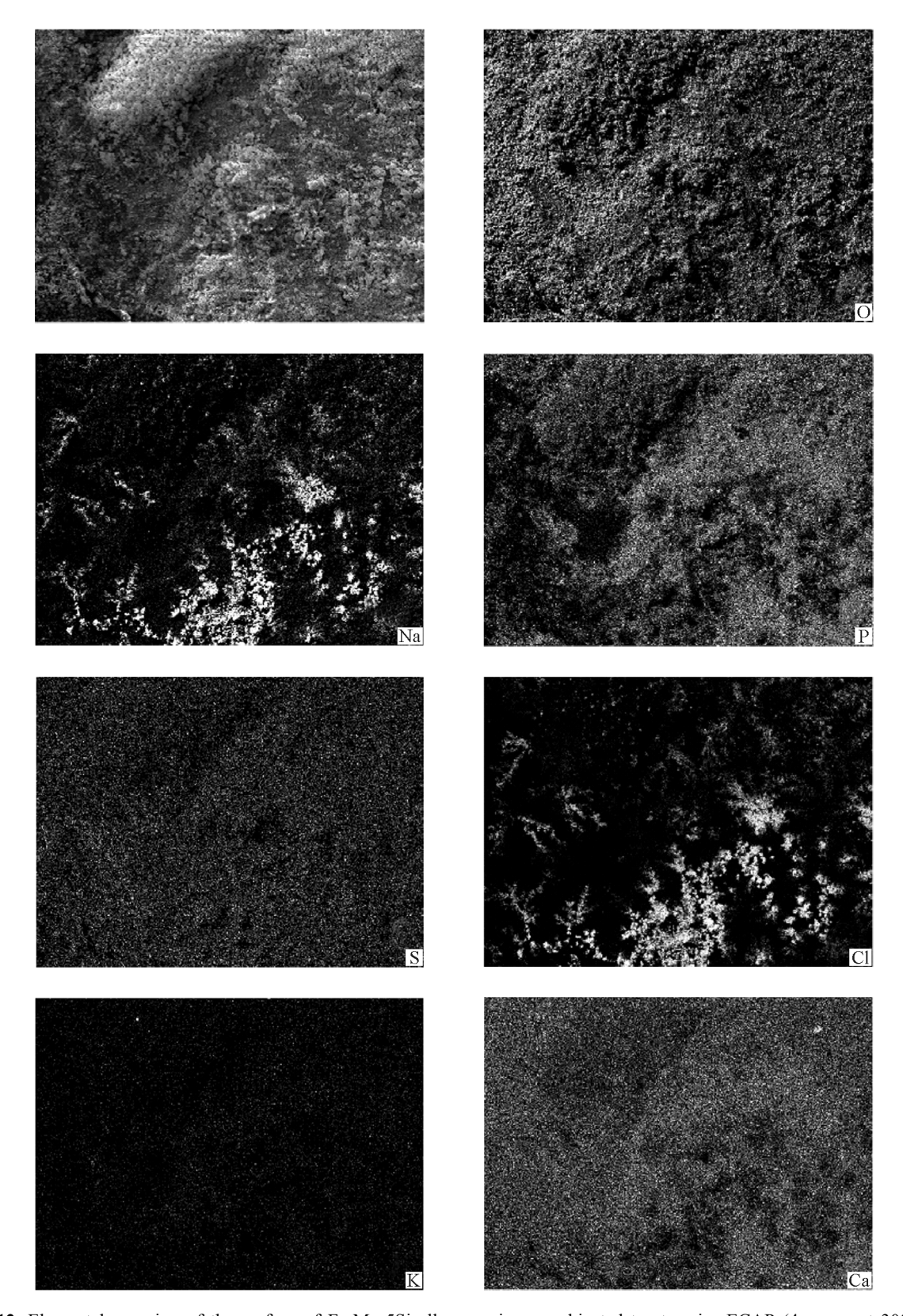


Fig. 12. Elemental mapping of the surface of Fe-Mn-5Si alloy specimens subjected to stepwise ECAP (4 passes at $300^{\circ}\text{C} + 1$ pass at 450°C) after 14-day incubation in DMEM.

and silicon shifts the corrosion potential E to the negative region from $E = -0.61 \,\text{V}$ for annealed commercially pure iron to E = -0.78 and $-0.82 \,\text{V}$ for Fe-Mn-5Si and Fe-Mn-3.7Si in the annealed state, respectively (Fig. 9). This indicates an increase in the susceptibility of the studied alloys to corrosion.

Nevertheless, the corrosion rate of Fe-Mn-3.7Si and Fe-Mn-5Si alloys is about 0.21 mm/year. Figure 10 shows a diagram comparing the corrosion potential and the electrochemical corrosion rate for the studied alloys after various treatments, whose values are lower than even the corrosion rate of commercially pure iron (0.23 mm/year). Ferrite (the phase state of commercially pure iron) is more corrosion-resistant than austenite (the phase state of Fe-Mn-3.7Si and Fe-Mn-5Si alloys after annealing and ECAP).

This behavior indicates the influence of the alloy structure rather than of the chemical composition. It is known that, in Fe-based alloys with an fcc lattice, twin boundaries are low-energy special boundaries that increase the corrosion resistance in contrast to the high-energy twin boundaries of Mg alloys [31]. In this case, the presence of annealing twins in the austenitic structure of Fe-Mn-3.7Si and Fe-Mn-5Si allovs significantly increases the corrosion resistance of the alloy. Severe plastic deformation of alloys by ECAP in most modes increases the corrosion rate, while it has virtually no effect on the corrosion potential. For alloys where austenite is structurally heterogeneous and is characterized by the presence of twins, the corrosion rate is low. In alloys doped with silicon, the structure formed after ECAP at 400°C has a significant density of twins and increases the corrosion rate to 0.33 mm/year for the Fe-Mn-3.7Si alloy and only to 0.26 mm/year for the Fe-Mn-5Si allov. Stepwise ECAP at 300°C with temperature increase to 450°C of the Fe-Mn-5Si alloy leads to the formation of a nanostructured austenitic state, thus increasing the corrosion rate by almost 2 times compared to austenite in the alloy after annealing and after ECAP at 400°C.

The results of immersion tests show (Fig. 11) that the alloys in all states have the highest corrosion rate after 1 day of incubation in the culture medium, which is close to that obtained by the potentiodynamic polarization method within the measurement error. Increasing the incubation time to 14 days significantly reduces the corrosion rate.

Elemental mapping of the corrosion products on the surface of the Fe-Mn-5Si specimen after stepwise ECAP at 300°C (4)+450°C (1) in vitro incubated in DMEM for 14 days reveals Ca²⁺, Na⁺, K⁺, Cl⁻, SO₄²⁻, PO₄³⁻ and HCO³⁻ ions, which are the medium components (Fig. 12). The presence of chlorine ions Cl⁻ destructs the protective layer of iron-based alloys, causing local pitting corrosion. Pitting damage complicates the removal of corrosion products and makes the calculation of the corrosion rate based on the results of long-term immersion tests incorrect.

4. CONCLUSIONS

The study of ultrafine-grained austenitic Fe-Mn-Si alloys obtained by ECAP revealed that this treatment ensured properties necessary for the manufacture of biocompatible biodegradable implantable devices. An exception is the shape memory effect, which was undetected in the temperature range close to the temperature of the human body. It was found that ECAP in the isothermal modes at 300 and 400°C and in the stepwise mode including 4 passes at 300°C and 1 pass at 450°C lead to the formation of an ultrafine-grained austenitic structure with twins of various density in the studied Fe-Mn-Si alloys. The resulting ultrafine-grained structure determined high strength characteristics $(1257 \le \sigma_B \le 1626 \text{ MPa}, 1084 \le \sigma_{0.2} \le 1402 \text{ MPa})$ at satisfactory ductility $(14 \le \delta \le 8.4\%)$.

The potentiodynamic polarization method demonstrated a significant decrease in the corrosion potential due to alloying of iron with manganese and silicon, which indicates an increase in the susceptibility of the studied alloys to corrosion. The presence of special twin boundaries in the structure of Fe-Mn-Si alloys increases the corrosion resistance of the alloys. The increased corrosion rate was revealed in the ECAP-treated alloys due to the formation of a predominantly grain-subgrain structure with a smaller number of twins $(0.38\pm0.04\,\mathrm{mm/year}$ for the Fe-Mn-3.7Si alloy after ECAP at 300°C and $0.4\pm0.06\,\mathrm{mm/year}$ for Fe-Mn-5Si after stepwise ECAP).

The shape memory effect in the studied alloys manifests itself at temperatures unacceptable for medical use. Structure refinement by ECAP in modes that provide a fully austenitic state decreased shape memory properties.

ACKNOWLEDGMENTS

The microstructure was studied using the equipment of the Shared Facility Centre for Studies of HTS and Other Strongly Correlated Materials (SFC LPI). Transmission electron microscopy was performed using the equipment of Materials Science and Metallurgy Shared Use Center.

FUNDING

The work was supported by Russian Science Foundation (project No. 23-23-00096).

CONFLICT OF INTEREST

The authors of this work declare that they have no conflicts of interest.

REFERENCES

- 1. Zheng, Y.F., Gu, X.N., and Witte, F., Biodegradable Metals, *Mater. Sci. Eng. R.*, 2014, vol. 77, pp. 1–34.
- 2. Heiden, M., Walker, E., and Stanciu, L., Magnesium, Iron and Zinc Alloys, the Trifecta of Bioresorbable Orthopaedic and Vascular Implantation—A Review, *J. Biotechnol. Biomater.*, 2015, vol. 5(2), pp. 1–9.
- Hussain, M., Khan, S.M., Al-Khaled, K., Ayadi, M., Abbas, N., and Chammam, W., Performance Analysis of Biodegradable Materials for Orthopedic Applications, *Mater. Today Commun.*, 2022, vol. 31, p. 103167. https://doi.org/10.1016/j.mtcomm.2022.103167
- Waksman, R., Pakala, R., Baffour, R., Seabron, R., Hellinga, D., and Tio, F.O., Short-Term Effects of Biocorrodible Iron Stents in Porcine Coronary Arteries, *J. Interv. Cardiol.*, 2008, vol. 21, pp. 15–20.
- Hermawan, H., Dubé, D., and Mantovani, D., Developments in Metallic Biodegradable Stents, *Acta Biomater.*, 2010, vol. 6, pp. 1693–1697.
- Moravej, M. and Mantovani, D., Biodegradable Metals for Cardiovascular Stent Application: Interests and New Opportunities, *Int. J. Mol. Sci.*, 2011, vol. 12, pp. 4250–4270.
- 7. Hermawan, H., Purnama, A., Dube, D., Couet, J., and Mantovani, D., Fe–Mn Alloys for Metallic Biodegradable Stents: Degradation and Cell Viability Studies, *Acta Biomater.*, 2010, vol. 6(5), pp. 1852–1860.
- 8. Hermawan, H., Dubé, D., and Mantovani, D., Development of Degradable Fe-35Mn Alloy for Biomedical Application, *Adv. Mater. Res.*, 2006, vol. 15–17, pp. 107–112. https://doi.org/10.4028/www.scientific.net/amr.15-17.107
- 9. Hermawan, H., Dubé, D., and Mantovani, D., Degradable Metallic Biomaterials: Design and Development of Fe–Mn Alloys for Stents, *J. Biomed. Mater. Res. A*, 2010, vol. 93(1), pp. 1–11.
- 10. Liu, B. and Zheng, Y., Effects of Alloying Elements (Mn, Co, Al, W, Sn, B, C and S) on Biodegradability and In Vitro Biocompatibility of Pure Iron, *Acta Biomater.*, 2011, vol. 7(3), pp. 1407–1420.
- 11. Cheng, J., Liu, B., Wu, Y.H., and Zheng, Y.F., Comparative In Vitro Study on Pure Metals (Fe, Mn, Mg, Zn and W) as Biodegradable Metals, *J. Mater. Sci. Technol.*, 2013, vol. 29(7), pp. 619–627. https://doi.org/10.1016/j.jmst.2013.03.019

- Schinhammer, M., Hänzi, A.C., Löffler, J.F., and Uggowitzer, P.J., Design Strategy for Biodegradable Fe-Based Alloys for Medical Applications, *Acta Biomater.*, 2010, vol. 6(5), pp. 1705–1713. https://doi.org/10.1016/j.actbio.2009.07.039
- Moszner, F., Sologubenko, A.S., Schinhammer, M., Lerchbacher, C., Hänzi, A.C., Leitner, H., Uggowitzer, P.J., and Löffler, J.F., Precipitation Hardening of Biodegradable Fe–Mn–Pd Alloys, *Acta Mater.*, 2011, vol. 59, pp. 981–991. https://doi.org/10.1016/j.actamat. 2010.10.025
- Rybalchenko, O., Anisimova, N., Martynenko, N., Rybalchenko, G., Kiselevskiy, M., Tabachkova, N., Shchetinin, I., Raab, A., and Dobatkin, S., Structure Optimization of a Fe–Mn–Pd Alloy by Equal-Channel Angular Pressing for Biomedical Use, *Materials*, 2023, vol. 16, p. 45. https://doi.org/10.3390/ma16010045
- Liu, B., Zheng, Y.F., and Ruan, L., In Vitro Investigation of Fe30Mn6Si Shape Memory Alloy as Potential Biodegradable Metallic Material, *Mater. Lett.*, 2011, vol. 65(3), pp. 540–543. https://doi.org/10.1016/j.mat let.2010.10.068
- Sato, A., Yamaji, Y., and Mori, T., Physical Properties Controlling Shape Memory Effect in Fe-Mn-Si Alloys, *Acta Metall.*, 1986, vol. 34, pp. 287–294. https://doi. org/10.1016/0001-6160(86)90199-9
- 17. Vintaikin, E.Z., Gulyaev, A.A., Oralbaev, A.B., Polyakova, N.A., and Svistunova, E.L., On the Nature of the Shape Memory Effect in Fe-Mn-Si Alloys, *Metallofizika*, 1991, vol. 13(8), pp. 43–51.
- 18. Sato, A., Chishima, E., Soma, K., and Mori, T., Shape Memory Effect in γ ↔ ε Transformation in Fe-30Mn-1Si Alloy Single Crystals, *Acta Metall.*, 1982, vol. 30(6), pp. 1177–1183. https://doi.org/10.1016/0001-6160(82)90011-6
- Sato, A., Chishima, E., Yamaji, Y., and Mori, T., Orientation and Composition Dependencies of Shape Memory effect in Fe-Mn-Si Alloys, *Acta Metall.*, 1984, vol. 32(4), pp. 539–547. https://doi.org/10.1016/0001-6160(84)90065-8
- 20. Bohner, M., Silicon-Substituted Calcium Phosphates—A Critical View, *Biomaterials*, 2009, vol. 30, pp. 6403–6406. https://doi.org/10.1016/j.biomaterials. 2009.08.007
- Khan, A.F., Saleem, M., Afzal, A., Ali, A., Khan, A., and Khan, A.R., Bioactive Behavior of Silicon Substituted Calcium Phosphate Based Bioceramics for Bone Regeneration, *Mater. Sci. Eng. C*, 2014, vol. 35, pp. 245–252. https://doi.org/10.1016/j.msec.2013.11.013
- 22. Lin, H.C., Lin, K.M., Lin, S., and Ouyang, T.M., The Corrosion Behavior of Fe-Based Shape Memory Alloys, *Corrosion Sci.*, 2002, vol. 44(9), pp. 2013–2026. https://doi.org/10.1016/S0010-938X(02)00027-6
- 23. Fantanariu, M., Trinca, L.C., Solcan, C., Trofin, A., Strungaru, S., Sindilar, E.V., Plavan, G., and Stan-

- ciu, S., A New Fe-Mn-Si Alloplastic Biomaterial as Bone Grafting Material: In Vivo Study, *Appl. Surf. Sci.*, 2015, vol. 352, pp. 129–139. https://doi.org/10.1016/j.apsusc.2015.04.197
- 24. Trinca, L.C., Burtan, L., Mareci, D., Fernandez-Perez, B.M., Stoleriu, I., Stanciu, T., Stanciu, S., Solcan, C., Izquierdo, J., and Souto, R.M., Evaluation of In Vitro Corrosion Resistance and In Vivo Osseointegration Properties of a Fe-Mn-Si-Ca Alloy as Potential Degradable Implant Biomaterial, *Mater. Sci. Eng. C*, 2021, vol. 118, p. 111436. https://doi.org/10.1016/j.msec.2020.111436
- Drevet, R., Zhukova, Y., Malikova, P., Dubinskiy, S., Korotitskiy, A., Pustov, Y., and Prokoshkin, S., Martensitic Transformations, Mechanical and Corrosion Properties of Fe-Mn-Si Alloys for Medical Implant Applications, *Metall. Mater. Trans. A*, 2018, vol. 49, pp. 1006–1013.
- Pustov, Y.A., Zhukova, Y.S., Malikova, P.E., Prokoshkin, S.D., and Dubinskii, S.M., Structure and Corrosion-Electrochemical Behavior of Bioresorbable Alloys Based on the Fe–Mn System, *Prot. Met. Phys. Chem. Surf.*, 2018, vol. 54, pp. 469–476. https://doi. org/10.1134/S2070205118030139
- Prokoshkin, S., Pustov, Y., Zhukova, Y., Kadirov, P., Karavaeva, M., Prosviryakov, A., and Dubinskiy, S., Effect of Thermomechanical Treatment on Structure and Functional Fatigue Characteristics of Biodegradable Fe-30Mn-5Si (wt %) Shape Memory Alloy, *Materials*, 2021, vol. 14, p. 3327. https://doi.org/10.3390/ma14123327

- Prokoshkin, S., Pustov, Y., Zhukova, Y., Kadirov, P., Dubinskiy, S., Sheremetyev, V., and Karavaeva, M., Effect of Thermomechanical Treatment on Functional Properties of Biodegradable Fe-30Mn-5Si Shape Memory Alloy, *Metall. Mater. Trans. A*, 2021, vol. 52.
- Rybalchenko, O., Anisimova, N., Martynenko, N., Rybalchenko, G., Belyakov, A., Shchetinin, I., Lukyanova, E., Chernogorova, O., Raab, A., Pashintseva, N., Kornyushenkov, E., Babaeva, G., Sokolova, D., Kiselevskiy, M., and Dobatkin, S., Biocompatibility and Biodegradation In Vitro and In Vivo of Fe-Mn-5Si Alloy Strengthened by Equal Channel Angular Pressing, *Appl. Sci.*, 2023, vol. 13(17), p. 9628. https://doi.org/10.3390/app13179628
- Schuck, G., Iwata, A., Sasaki, A., Himeda, A., Konaka, H., and Muroyama, N., Crystal Structure Analysis Using Integrated X-Ray Powder Diffraction Software Suite PDXL, *Acta Crystallogr. A*, 2010, vol. 66, p. 311.
- 31. Gerashi, E., Alizadeh, R., and Langdon, T.G., Effect of Crystallographic Texture and Twinning on the Corrosion Behavior of Mg Alloys: A Review, *J. Magnes. Alloy*, 2022, vol. 10(2), pp. 313–325.

Publisher's Note. Pleiades Publishing remains neutral with regard to jurisdictional claims in published maps and institutional affiliations. AI tools may have been used in the translation or editing of this article.